Composites Part C: Open Access 13 (2024) 100426

Contents lists available at ScienceDirect

Composites Part C: Open Access

journal homepage: www.elsevier.com/locate/composites-part-c-open-access

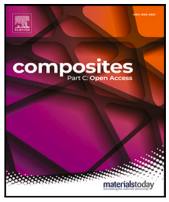

# Experimental investigation on low-velocity impact behavior of glass, Kevlar, and hybrid composites with an elastomeric polyurethane matrix

Alessandro Vescovini [a], Joziel A. Cruz [b], Dayou Ma [a], Chiara Colombo [a], Antonio Salerno [c], Otavio Bianchi [b], Sandro C. Amico [b], Andrea Manes [a,*]

[a] Politecnico di Milano, Department of Mechanical Engineering, Milan, Italy
[b] Federal University of Rio Grande do Sul, Porto Alegre, Brazil
[c] Politecnico di Milano, Department of Energy, Milan, Italy

ARTICLE INFO

*Keywords:*
Low-velocity impact
Hybrid composite
Thermography
Elastomeric matrix

ABSTRACT

Low-velocity impacts represent a critical dynamic condition for engineering structures. Combining two reinforcing fibers in a single matrix, i.e., hybridization, is considered a feasible way to improve composite performance. In this context, this paper presents an experimental work on composites with Kevlar and glass fabrics and a novel thermoset polyurethane matrix. The coupons are manufactured by vacuum infusion technique and low-velocity impact tests are carried out. First, the impact behavior of Kevlar and glass laminates of different thicknesses is assessed, and then impact tests are performed on different configurations of hybrid laminates, both symmetric and non-symmetric. For the non-symmetric specimens, impact tests were conducted on both sides of the stack. Load vs displacement curves are reported along with absorbed energy. To investigate the damage mechanism, the front, back, and cross-section views of the specimens are analyzed, and features related to the stacking sequences are discussed. Thermographic analyses are carried out on the impacted specimens to further analyze damage. The failure mechanisms are different from traditional epoxy composites and a hybridization effect is reported. The results evidence that the hybrid coupons are viable for structural applications, being capable of absorbing high-impact energies, in particular, non-symmetric hybrid laminates outperformed the Kevlar, glass, and symmetric ones, absorbing roughly 15% less energy for the highest energy impact.

## 1. Introduction

A well-known limitation associated with the use of composite materials is their vulnerability to impacts occurring in directions perpendicular to their plane, which can deteriorate mechanical properties and structural safety, even for low-energy impacts. Researchers have extensively investigated their response to low-velocity impacts [1,2], exploiting both numerical analyses and experimental tests to support the discussion on the composite damage [3,4]. The performance of these composites can be improved by using multiple types of reinforcing fibers within a single matrix, a strategy known as hybridization, which has been identified as a pragmatic approach to address this challenge [5,6].

Numerous investigations have delved into the low-velocity impact characteristics of epoxy hybrid composites comprising carbon, glass, and epoxy. These studies primarily aim to reduce costs while preserving or enhancing the properties. Hosur et al. [5] experimentally assessed the impact behavior of various twill weave carbon/S2-glass fabric hybrids and revealed a substantial enhancement in damage tolerance with hybridization, by having S2-glass fabrics on the back surface and twill-weave carbon on the front surface, impact response of the hybrid laminates was enhanced because S2-glass fibers have higher strain to failure. Sayer et al. [7] studied the low-velocity impact behavior of 50 K carbon fabrics/unidirectional (UD) E-glass fabrics epoxy hybrid composites, showing that the perforation threshold of hybrids with carbon fibers on the impacted surface was approximately 30% higher than that with glass fibers. González et al. [8] conducted an experimental study involving woven glass and carbon fabrics, and UD carbon tape, and highlighted that the arrangement of layers within the hybrid structure significantly influenced the impact response, favoring the use of glass fabric in the core of the laminate. This would reduce the dissipation and increase the CAI strength since the threshold load is delayed to higher impact energies. Likewise, Wagih et al. [9] investigated the low-velocity impact of plain weave carbon-aramid/epoxy hybrid composites and the flexural strength, emphasizing the improvement

* Corresponding author.
*E-mail address:* andrea.manes@polimi.it (A. Manes).

https://doi.org/10.1016/j.jcomc.2023.100426
Received 6 October 2023; Received in revised form 13 December 2023; Accepted 13 December 2023
Available online 16 December 2023
2666-6820/© 2023 The Author(s). Published by Elsevier B.V. This is an open access article under the CC BY license (http://creativecommons.org/licenses/by/4.0/).

in residual strength by placing a tougher aramid layer in the core of the laminate. Researchers have investigated different configurations of hybrid composites, Zhang et al. [10] examined composites constituted of warp-knitted carbon and glass fabrics and reported that the intra-layer hybrid structure enhanced resistance to crack propagation and low-velocity impact performance. Kazemi et al. [11] observed a decrease in structural loss and absorbed energy of up to 47% and 18%, respectively, when changing from carbon fabrics to ultra-high-molecular-weight polyethylene (UHMWPE) fabrics on the impacting side of hybrid laminates. Barouni et al. [12] studied the impact response of glass, glass-flax, and flax composites through a combination of experimental and numerical observations. The introduction of glass fibers into a flax fiber laminate significantly improved impact load capability and absorbed energy. Regarding the use of natural fibers, Al-Shamary et al. [13] utilized male palm fiber together with glass layers stitched at [0°/90°] to enhance the impact properties. The composite was produced using vacuum infusion molding and they demonstrated that the incorporation of palm fibers in glass/epoxy composites significantly improved energy absorption and delayed the onset of damage modes. The choice of fabric type influenced failure types and impact performance [14], and the incorporation of glass fibers on the impact side had a positive effect on energy absorption and peak impact force of a carbon–glass epoxy hybrid [15].

In addition, the impact behavior of glass/epoxy laminates and the influence of temperature on punch shear and low-velocity impact performance have been explored in recent studies. The work by Aktas et al. [16] delves into the impact behavior of laminated glass/epoxy composite plates with $[0/90/0/90]_S$ and $[0/90/+45/-45]_S$ stacking sequences at room temperature, 60 °C and 100 °C. The authors reported an increase in the perforation threshold with rising temperatures, providing valuable insights into the material's response under different thermal conditions. Furthermore, Karakuzu et al. [17] studied S2-glass fabric and carbon-kevlar hybrid fabric-reinforced epoxy composites, investigating both quasi-static and low-velocity impact tests at various temperatures. The results revealed temperature-dependent variations in maximum contact force, damage modes, and perforation energy of the composite.

Glass-aramid hybrid composites are being increasingly investigated. Recent studies by Da Silva et al. [18,19] focused on both quasi-static and ballistic properties of plain-weave aramid/glass fabric/epoxy composites. Hybridization showed the potential to enhance energy absorption. However, the hybrid laminates displayed lower ballistic limit velocities compared to their single-fiber counterparts. Vescovini et al. [20] replicated Da Silva et al. tests in a numerical framework to investigate the hybridization effect, utilizing a finite element model with sensitivity to strain rate in LS-DYNA software, and highlighted the capability to predict hybridization effect of the proposed framework. Rezasefat et al. [21] carried out an experimental campaign to assess the hybridization effect in plain-weave Kevlar 29® and 8-harness satin S2-glass fabrics interply epoxy composites, investigating both symmetric and non-symmetric laminates. They observed changes in damage morphology and enhanced impact performance from hybridization, even though the glass laminate performed better at high-impact energies. They also consistently reported higher maximum impact force for specimens with glass layers on the impact side. Furthermore, Rezasefat et al. [22] proposed a multi-criteria decision-making analysis to determine the optimal laminate design, based on the technique for order of preference by similarity to the ideal solution and proposed a novel finite element model using continuum damage mechanics, considering non-linear material behavior and accounting for various inter-laminar and intra-laminar failure modes. They found that single-fiber laminates exhibited the least favorable design characteristics, whereas hybrid laminates featuring aramid layers on the impact side were the optimal design.

More recently, the scientific community in the field of composite materials has focused on other matrices rather than traditional thermosets. For instance, thermoplastics, have potential benefits in terms of mechanical properties (e.g., improved toughness), paving new manufacturing routes, and improving sustainability of composite materials. Vieille et al. [23] compared the impact performance and susceptibility to barely visible impact damage of carbon woven composites with epoxy, polyether ether ketone (PEEK), and polyphenylene sulfide (PPS) matrix, and they observed significant differences in damage mechanism for thermoset and thermoplastic matrices. They identified advantageous features due to the inherent toughness of the fabric, such as the availability of matrix-rich regions at the fiber bundles crimp where plastic deformation can develop, and crack propagation along the curved yarns. Polyurethane (PU) is being increasingly adopted for engineering applications, and according to the chemical structure, it may display thermoplastic, elastomeric, or thermoset behavior [24]. In a recent study by Cruz et al. [25], they conducted a comprehensive characterization of Kevlar, glass, and hybrid woven composites manufactured using a specially formulated PU resin. The PU resin was created through a crafted blend of polyols, designed to precisely adjust the infusion molding parameters. Their investigation focused on mechanical properties with dynamic-mechanical analysis, static tests, and quasi-static indentation tests. The findings suggest that the newly developed resin holds promise for enhancing impact absorption in various applications, such as protective armor. Other researchers investigated the effect of a PU matrix in low-velocity impact tests. Zhao et al. [26] studied the low-velocity impact resistance of warp-knitted fabric composites with flexible PU matrix and demonstrated that the damage morphology is significantly related to the shape of the punch, and reported failure mechanisms such as fiber fracture, interfacial debonding, and matrix cracks. Nicholas et al. [27] studied the microstructure of thermoset PU composite and reported that the bulk composite material was resistant to UV aging, with no relevant changes in impact properties.

The scientific literature reports a few works investigating low-velocity impact on composites manufactured with matrices other than epoxy, but attention is shifting towards other resins, aiming at improving the performance and reliability of composite structures. The works presented here showed promising prospects and highlighted potential benefits from other resins. Therefore, building on a previous experimental campaign that investigated the effect of hybridization with Kevlar and glass hybrid epoxy composites [21], this paper focuses on the low-velocity impact behavior of composites produced with a recently developed thermoset elastomeric PU resin [25,28]. Kevlar and glass composite coupons of varying thickness, as well as different configurations of symmetric and non-symmetric hybrid composites of similar areal density are studied. In Section 2 the specimens and the experimental procedure are presented. In Section 3, the experimental results related to the Kevlar, the glass, and the hybrid composites are shown, and the effect of the material on the impact side is discussed. Finally, the paper concludes in Section 4. For the sake of brevity and readability, some of the results are reported in Appendix.

## 2. Materials and methods

### 2.1. Materials and specimens preparation

The specimens for the tests presented in this study are manufactured at the Federal University of Rio Grande do Sul. Plain-weave Kevlar 29® fabrics (440 g/m$^2$, 0.62 mm, 7 threads/cm, $\rho$ = 1.45 g/cm$^3$) from Dupont [29] and 8-harness satin S2-glass fabrics (302 g/m$^2$, 0.24 mm, 22 threads/cm, 2.49 g/cm$^3$) from Hexcel [30] are used. The matrix of the composites is an elastomeric polyurethane (PU) with a density of 1.05 g/cm$^3$. The polyurethane resin comprises a blend (50/50 by weight) of castor oil with a hydroxyl value of 160 mg KOH/g and a functionality of 2.7, and polypropylene oxide (PPO) with a hydroxyl value of 110 mg KOH/g and a functionality of 2.0. This mixture was polymerized with polymeric isocyanate 4,4'-diphenylmethane diisocyanate (pMDI) with a functionality of 2.7 and a free isocyanate index

**Table 1**
Glass and Kevlar specimens.

| Specimen | Thickness [mm] | Areal density ($\rho_a$) [g/cm$^2$] |
|---|---|---|
| [$K_5$] | 2.83 | 0.31 |
| [$K_8$] | 4.42 | 0.51 |
| [$K_{13}$] | 6.75 | 0.80 |
| [$K_{18}$] | 9.42 | 1.09 |
| [$G_8$] | 2.48 | 0.32 |
| [$G_{10}$] | 3.28 | 0.43 |
| [$G_{15}$] | 3.96 | 0.63 |
| [$G_{20}$] | 6.39 | 0.82 |

**Table 2**
Glass-Kevlar hybrid specimens.

| Specimen | Thickness [mm] | Areal density ($\rho_a$) [g/cm$^2$] | Aramid layer ratio ($n_K/n_G$) [ ] | Aramid ratio ($\rho_{a,K} n_K/\rho_a$) [ ] |
|---|---|---|---|---|
| $[G_4/K_2]_S$ | 4.72 | 0.57 | 0.50 | 0.43 |
| $[G_2/K]_{2S}$ | 4.55 | 0.57 | 0.50 | 0.42 |
| $[K_2/G_4]_S$ | 4.22 | 0.57 | 0.50 | 0.43 |
| $[G_8/K_4]$ | 4.83 | 0.57 | 0.50 | 0.43 |
| $[G_6/K_5]$ | 4.38 | 0.57 | 0.83 | 0.54 |

of 31.40 ± 0.02 wt%. The preparation of these materials followed established procedures outlined in the literature [28]. Before manufacturing the composites, the fabric layers are dried in an oven at 120 °C for 12 h. The fabrics (310 mm × 460 mm) are stacked in a layup on the one-sided mold, and a layer of peel ply is added. A flow mesh is placed on top to promote resin distribution. The system is sealed using tacky tape, and the cavity is evacuated to remove air and compact the layers. The PU resin is introduced into the cavity through an inlet under a vacuum pressure of 1 bar, ensuring proper wetting of the layers. The material is left to cure for 12 h under vacuum, after which the laminate is extracted. Subsequently, the composite undergoes post-curing for 8 h at 65 °C to complete the PU polymerization. Finally, the plates are cut using water-jet [25] to produce rectangular specimens (100 mm × 150 mm) commonly adopted for low-velocity impact tests [31].

Table 1 presents the Kevlar and glass composite specimens investigated in this work, reporting average thickness and areal density, calculated as the weight of the specimen divided by its area. The average ply thickness (ratio between thickness and number of plies) is 0.54 ± 0.02 mm and 0.31 ± 0.01 mm, while the average ply areal density is 0.061 ± 0.001 g/cm$^2$ and 0.042 ± 0.002 g/cm$^2$ for the Kevlar and glass composites, respectively.

Table 2 presents all hybrid specimens, and the first letter in the stacking sequence indicates the layer facing the impactor. The aramid layers ratio is evaluated as the ratio between the number of Kevlar and glass layers ($n_K/n_G$), and the aramid ratio as the average Kevlar layer areal density multiplied by the number of Kevlar layers, normalized by the average areal density of the specimens ($\rho_{a,K} n_K/\rho_a$). The average areal density of a Kevlar layer is evaluated as the average of the value measured for all Kevlar specimens.

Finally, in Fig. 1 the stacking sequence of the laminates is schematically represented, where the yellow and gray bars indicate Kevlar and glass layers, respectively.

### 2.2. Material testing

Low-velocity impact tests are carried out at Politecnico di Milano using a StepLab DW1000 drop-tower, specifically designed for testing according to ASTM D7136 [31]. The testing apparatus employs a piezoelectric load cell instrumented on a hemispherical impactor having a 16 mm diameter. The acquisition frequency is set to 3 MHz, and a low-pass filter at 50 kHz is automatically applied by the software of the testing machine. The impact always occurs at the center of the coupon. The impactor velocity is measured with an optical sensor just before

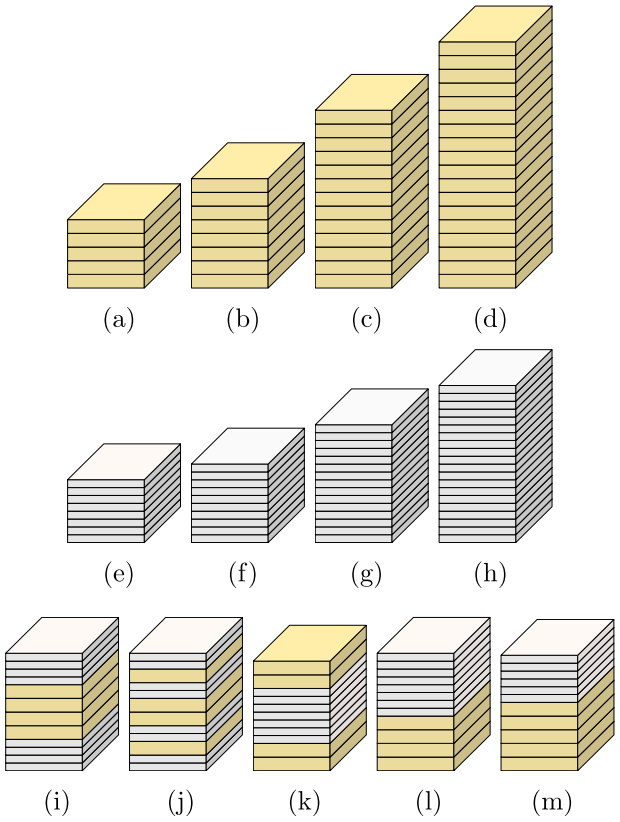


**Fig. 1.** Schematic representation of the specimens stacking sequence: (a) [$K_5$], (b) [$K_8$], (c) [$K_{13}$], (d) [$K_{18}$], (e) [$G_8$], (f) [$G_{10}$], (g) [$G_{15}$], (h) [$G_{20}$], (i) $[G_4/K_2]_S$, (j) $[G_2/K]_{2S}$, (k) $[K_2/G_4]_S$, (l) $[G_8/K_4]$, (m) $[G_6/K_5]$.

impact. The impact energies investigated are: 48.8 ± 0.4 J, 86.2 ± 0.4 J and 115.3 ± 0.9 J. The mass of the impactor for the former two energies is 6938.7 g, and 11898.2 g for the latter.

A single impact is carried out at each energy level. All specimens were tested at 49 J, 86 J, and 115 J (rounded values), except: 1) [$K_5$] that was not tested beyond 86 J due to the associated large damage that was already reached at that energy level, and the inability to guarantee the boundary conditions at larger impact energies; 2) [$K_4/G_8$] that was not tested at 49 J because of the limited number of specimens, 3) [$K_{18}$] was not tested at 49 J since no damage could be seen on this thick specimen, even for the impact at 86 J.

Based on preliminary tests carried out on the coupons, and previous work with composites manufactured with this matrix [25], it was designed *in-house* a fixture able to ensure that the coupons are firmly clamped. Fig. 2(a) shows the complete fixture assembly, with eight M22 bolts to keep the coupon in its position. Fig. 2(b) shows a detailed 3D model, highlighting the cross-section of the assembly before tightening the bolts, showing the threaded pins employed to further ensure that the coupons do not slip under impact.

To assess impact damage, infrared (IR) thermography is adopted. The 1 kW halogen lamp, model PLC64AL by Proel S.p.a., is used as the continuous heating source. The surface thermal transient is recorded with the IR camera Titanium by Cedip FLIR LLC, having an InSb cooled sensor with a Noise Equivalent Temperature Difference (NETD) smaller than 25 mK. Due to the low thermal diffusivity, the images were acquired for approximately 60 s, at a 2 Hz frame rate. Depending on the specimen, thermographic tests were performed both in transmission and in reflection. The thermographic data collection is carried out in transmission when the surface layer is glass fibers, and reflection when it is Kevlar, due to the different thermal transmittance of the surface material. The data acquired by the IR camera are post-processed

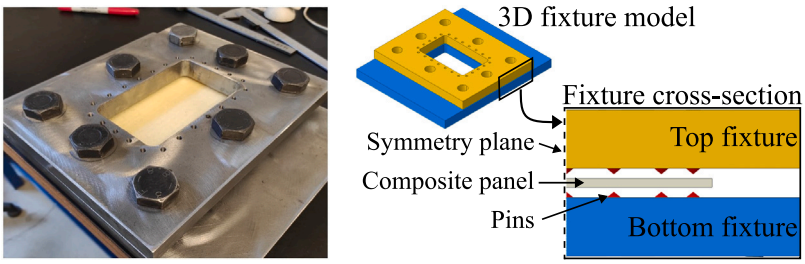


**Fig. 2.** (a) Experimental fixture, and (b) 3D model showing a cross-section view of the assembly.

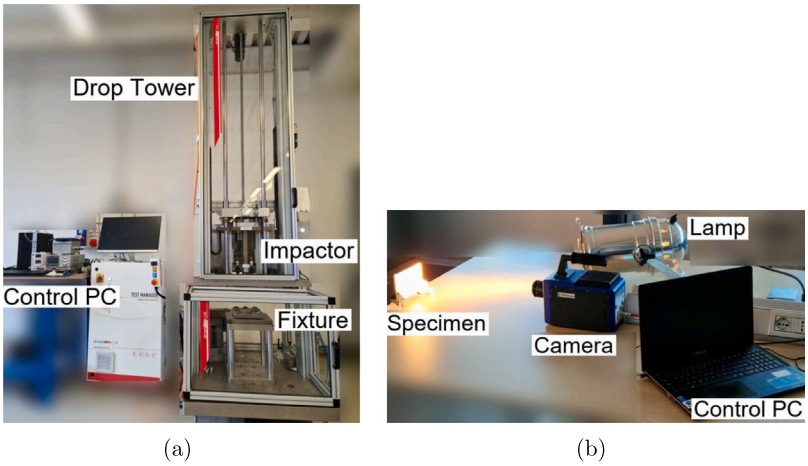


**Fig. 3.** Experimental setup for (a) the low-velocity impact and (b) thermography tests.

**Table 3**
Summary of the time parameters considered for IR thermography.

| | $t_0$ [s] | $t_j$ [s] | $t_i$ [s] |
|---|---|---|---|
| Transmitted thermal transient | 0 | 10 | 50 |
| Reflected thermal transient | 0 | 8 | 30 |

with a Python script. When transmitted thermal transient is recorded, the image is normalized as $T = T_i - T_j$, while for reflected thermal transient, the image is normalized as $T = (T_i - T_0)/(T_j - T_0)$ [32]; where $T$ represents thermal matrices, i, j, and 0 refer to times (t) of the acquisition, and $t_i > t_j > t_0$. $t_0$ is taken a time before the start of the heating process. The time $(t_i, t_j, t_0)$ considered for the thermal matrices does not depend on the different materials and thickness because no significant difference in the image was noted. In Table 3 the time values considered in the IR thermography are summarized.

Figs. 3(a) and 3(b) present the drop tower used for the experimental tests and the experimental setup for the thermographic tests, respectively.

After inspection, some specimens are cut with an automatic diamond saw blade in the middle, along the plane parallel to the short edge. Pictures of the cut face are taken with a Zeiss SteREO Discovery V12 stereomicroscope, to observe microscopic features of the damaged area.

## 3. Results and discussion

### 3.1. On the effect of composite thickness

The experimental load vs displacement curves recorded for Kevlar and glass composite coupons are presented in Fig. 4 and Fig. 5, respectively, for the impacts at 49 J, 86 J, and 115 J. The normalized absorbed energy, i.e., the ratio between absorbed energy, and impact energy, is reported in Fig. 6, and Table 4 summarizes the experimental results.

The stiffness of the specimens is consistent as the impact energy increases and maximum force and displacement increase accordingly. As expected, these parameters increase as a function of thickness. For

**Table 4**
Summary of impacts results for Kevlar and glass specimens.

| Specimens | | Maximum force [kN] | Maximum displacement [mm] | Absorbed energy [J] | Norm. abs. energy [J/J] |
|---|---|---|---|---|---|
| $[K_5]$ | 49 J | 5.82 | 19.79 | 38.72 | 0.79 |
| | 86 J | 7.62 | 25.60 | 74.20 | 0.86 |
| $[K_8]$ | 49 J | 7.31 | 15.26 | 38.14 | 0.80 |
| | 86 J | 9.64 | 19.05 | 74.86 | 0.87 |
| | 115 J | 11.11 | 21.38 | 104.99 | 0.90 |
| $[K_{13}]$ | 49 J | 7.80 | 12.52 | 32.64 | 0.66 |
| | 86 J | 11.42 | 16.46 | 60.60 | 0.70 |
| | 115 J | 12.62 | 18.73 | 92.68 | 0.80 |
| $[K_{18}]$ | 86 J | 12.40 | 12.53 | 62.80 | 0.73 |
| | 115 J | 15.38 | 13.44 | 87.26 | 0.75 |
| $[G_8]$ | 49 J | 5.52 | 21.23 | 38.95 | 0.79 |
| | 86 J | 6.78 | 26.62 | 75.68 | 0.88 |
| | 115 J | 8.12 | 29.99 | 113.98 | 0.99 |
| $[G_{10}]$ | 49 J | 6.74 | 17.32 | 33.44 | 0.68 |
| | 86 J | 8.67 | 21.30 | 70.28 | 0.81 |
| | 115 J | 9.07 | 111.92 | 95.56 | 1.00 |
| $[G_{15}]$ | 49 J | 6.97 | 16.15 | 31.29 | 0.63 |
| | 86 J | 9.73 | 19.30 | 61.15 | 0.71 |
| | 115 J | 9.98 | 23.02 | 96.05 | 0.83 |
| $[G_{20}]$ | 49 J | 7.68 | 14.96 | 31.16 | 0.63 |
| | 86 J | 10.76 | 18.25 | 57.91 | 0.67 |
| | 115 J | 12.57 | 20.42 | 88.90 | 0.77 |

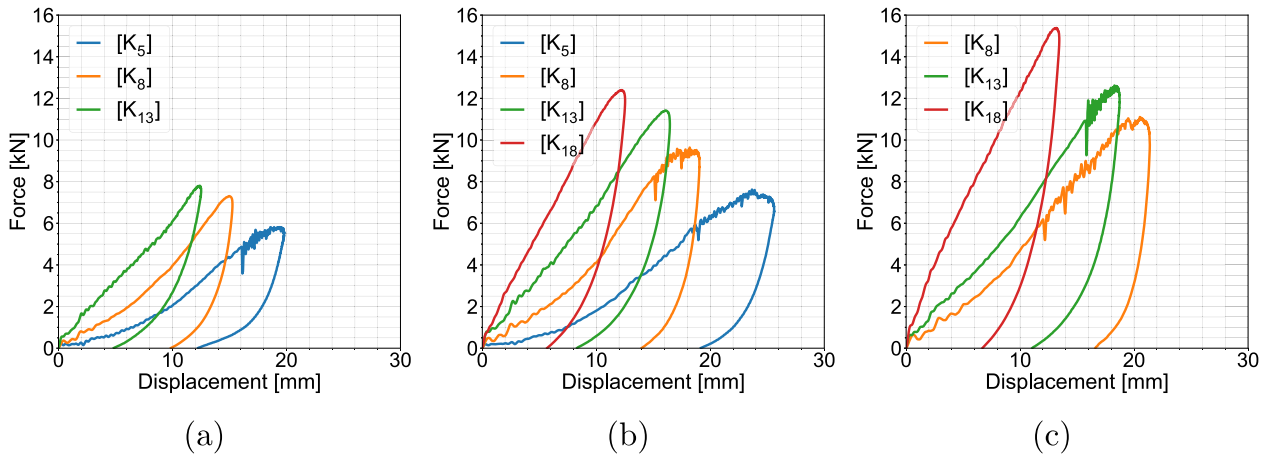


**Fig. 4.** Load vs. displacement curves of the Kevlar specimens impacted at (a) 49 J, (b) 86 J, and (c) 115 J.

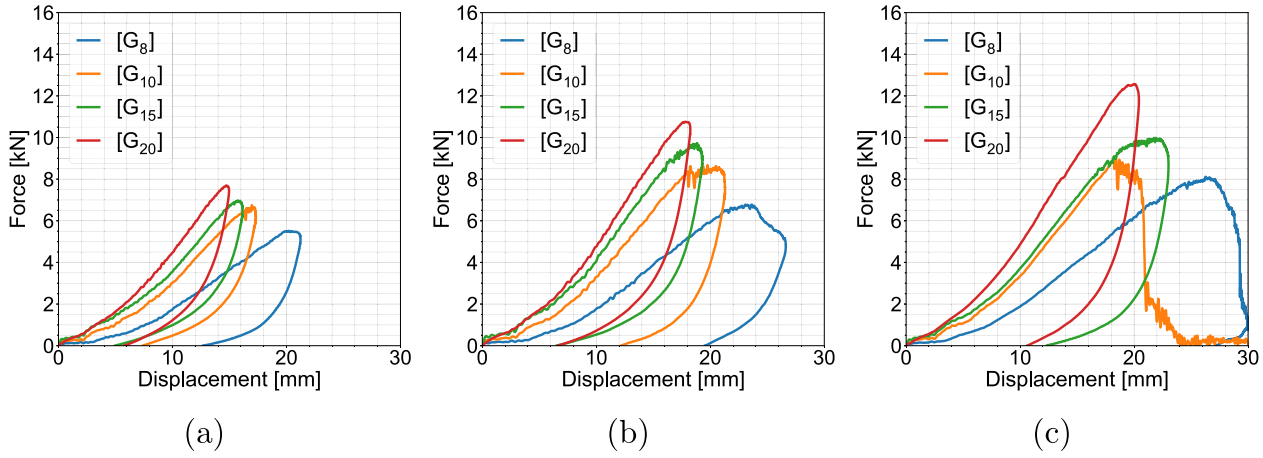


**Fig. 5.** Load vs. displacement curves of the glass specimens impacted at (a) 49 J, (b) 86 J, and (c) 115 J.

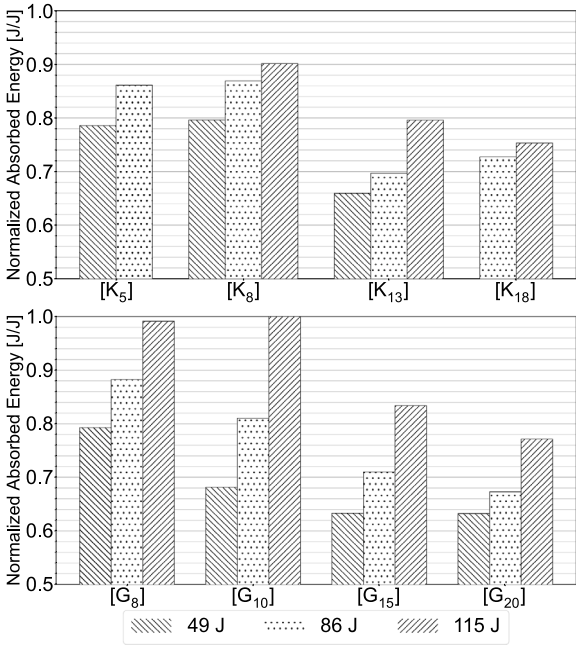


**Fig. 6.** Normalized absorbed energy of Kevlar and glass specimens.

all energy levels considered, the curves show a stiffening effect as the maximum force is approached, unlike previous studies where the curve is linear up to where damage occurs [21,23,33]. The difference can be attributed to different boundary conditions adopted in this work, compared to those indicated in the ASTM standard [31], and the contribution of membrane stiffness with large displacement [34,35]. Another remarkable difference is that a significant stiffness change usually occurs after a certain displacement and force, indicating damage in the specimen [33], while in the current results, this change is not reported; except for a few specimens, e.g., $[K_8]$ and $[G_{15}]$ for the impact at 115 J, where a short plateau is noted once the maximum force is reached. Comparing specimens with similar thickness and areal density, i.e., $[K_8]$–$[G_{15}]$ and $[K_{13}]$–$[G_{20}]$, no clear trend is observed regarding maximum force and displacement, while the absorbed energy is lower for the glass specimens, as reported for these same reinforcements with epoxy matrix [21], e.g., the glass coupons absorbed on average 14.9% and 4.4% less energy comparing $[K_8]$–$[G_{15}]$ and $[K_{13}]$–$[G_{20}]$, respectively.

In Fig. 7 different views of $[K_8]$ specimen tested at 115 J and $[G_{10}]$ specimen tested at 86 J are shown, respectively. The front and back views of $[G_{10}]$ specimen tested at 115 J are displayed in Fig. A.1 in the Appendix because the specimen was perforated, as indicated in Fig. 6, where this specimen absorbed nearly 100% of the impact energy. It is worth pointing out that both $[G_8]$ and $[G_{10}]$ specimens were perforated and only one of the specimens is reported in the Appendix. The two specimens do not recover the displacement like the others, as displayed in Fig. 5(c). For completeness, similar pictures of $[K_{13}]$ and

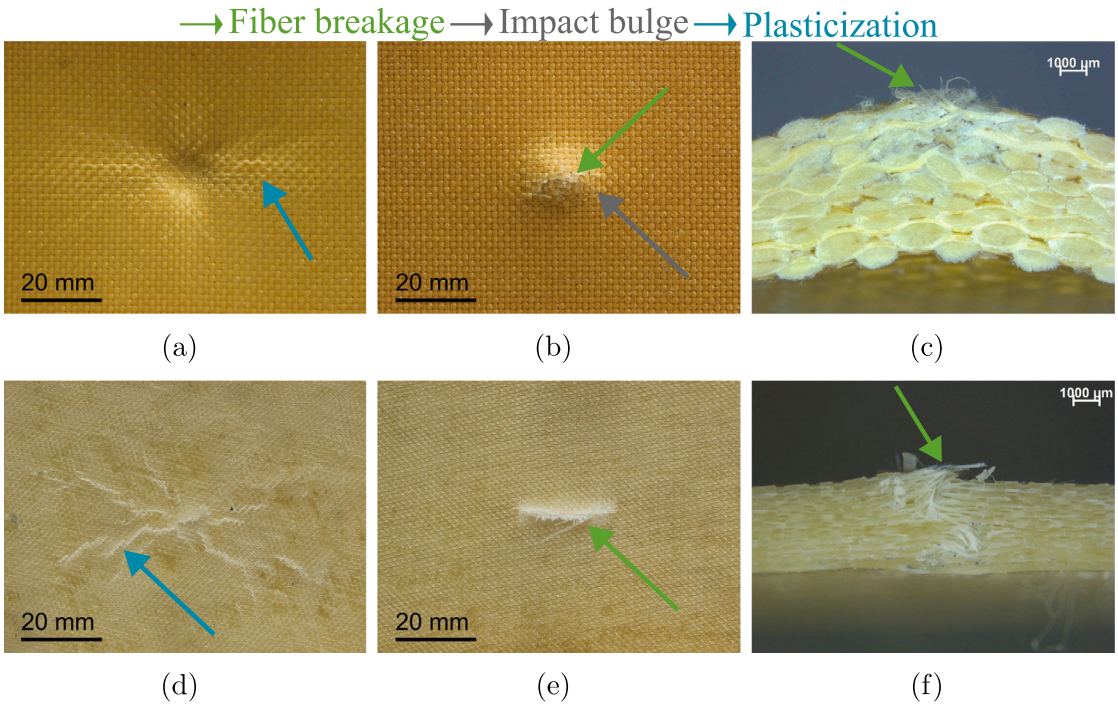


**Fig. 7.** Views of $[K_8]$ and $[G_{10}]$ specimens impacted at 86 J and 115 J, respectively: (a) front, (b) back, (c) cross-section views of the $[K_8]$ specimen, and (d) front, (e) back, (f) cross-section views of the $[G_{10}]$ specimen.

$[G_{15}]$ specimens are shown in Fig. A.2(a–c) and Fig. A.3(a–c) in the Appendix.

In Fig. 7(a), plastic deformation of $[K_8]$ specimen is seen near the impact location due to the through-the-thickness compression stress, whereas plasticization in the radial direction can be seen near the impact, due to the large strain the specimen undergoes at high impact energy. In Fig. 7(b), big bulge and fiber breakage are visible at the back, due to residual deformation resulting from the high tensile strain and plasticization of Kevlar. In the cross-section image, Fig. 7(c), the fiber breakage is visible for the layers from the middle plane outward. These damage mechanisms are typical of Kevlar specimens. In Fig. A.2(a–c), similar features can be seen for the thicker specimen, that is, plastic deformation and fiber breakage in the front and back views, although their extent is limited, as highlighted in the cross-section view. Regarding the $[K_5]$ specimen, the damage features presented in Fig. 7(a–c) are noted for that specimen even for impact at 86 J, and plastic deformation was noted close to the boundary condition, suggesting that a higher impact energy would affect the clamping area and compromise the boundary conditions. Instead, the $[K_{18}]$ specimen showed minimal damage at 86 J, therefore it was not tested at 49 J. Pictures of these specimens are omitted for conciseness.

In Fig. 7(d–f), the damage mechanisms of $[G_{10}]$ specimen present similarities to those of $[K_8]$. The front view in Fig. 7(d) shows extensive plasticization and yielded PU matrix along the radial direction, however, the residual compressive deformation is negligible compared to the $[K_8]$ specimen in Fig. 7(a). Fig. 7(e) shows fiber breakage in the back face of the specimens. And the cross-sectional view in Fig. 7(f), unlike the $[K_8]$ specimen, displays fiber breakage along the full thickness of the coupon, and the crack does not fall on a plane orthogonal to the specimen section, following instead an irregular path. In Fig. A.3, the thicker $[G_{15}]$ specimen show a comparable damage pattern.

The images in Fig. A.1 show a perforation mechanism similar to that reported by Rezasefat et al. for composites with epoxy matrix [21], however, in their case, the damage is more localized near the impact and the yielded matrix in the radial direction is not noted as in Fig. 7(d).

The damage mechanisms in the aramid and glass composites differ, distinct also from previous results with epoxy resin [21,36]. The impact side was always characterized by large plastic deformation and yielded matrix. Perforation was never visible except for a few cases in thin specimens impacted at high energy, i.e., $[G_8]$ and $[G_{10}]$ specimens. On the back side, the damage was more similar to that reported for epoxy composites, with fiber pullouts and cross or longitudinal cracks for the Kevlar and glass composites, respectively; only for very thick specimens, i.e., $[K_{18}]$ and $[G_{20}]$, no damage is reported in the back face. However, delamination was always negligible. This is the most striking feature shown by these specimens and confirms the advantages of using elastomeric polyurethane resin.

Thermographic analyses were carried out on the Kevlar and glass coupons. The front view in Fig. 8(a) clearly shows the impact site in yellow for $[K_8]$ specimen, while the plasticized area around it is darker than the rest of the specimen. The thermographic image of the back side of the same specimen, in Fig. 8(b), evidences with a dark color the fiber pullout in the outer fabric layers. The $[K_{13}]$ specimen shows similar features in the front view (Fig. A.2(d)), where the impact area is indicated with a white dashed circle and a darker area is seen around it. In Fig. A.2(e), the darker area represents fiber pullouts. However, the damage is less visible compared to Fig. 8(a, b), probably because the specimens are thicker, the Kevlar has low conductivity, and the extent of the damage is smaller. In Fig. 8(c), the crack at the center and the yielded marks surrounding the impact area at the front of the $[G_{10}]$ specimen are visible, similarly to the front of the $[G_{15}]$ specimen, presented in Fig. A.3(d).

### 3.2. On the effect of hybridization

The experimental load vs displacement curves for the hybrid composite coupons are presented in Fig. 9 for impacts at 49 J, 86 J, and 115 J. These specimens are selected because they have comparable thickness and areal density (see Table 2) and serve well for evaluating the effect of hybridization. The normalized absorbed energy is reported in Fig. 10, and in Table 5 the experimental results are summarized.

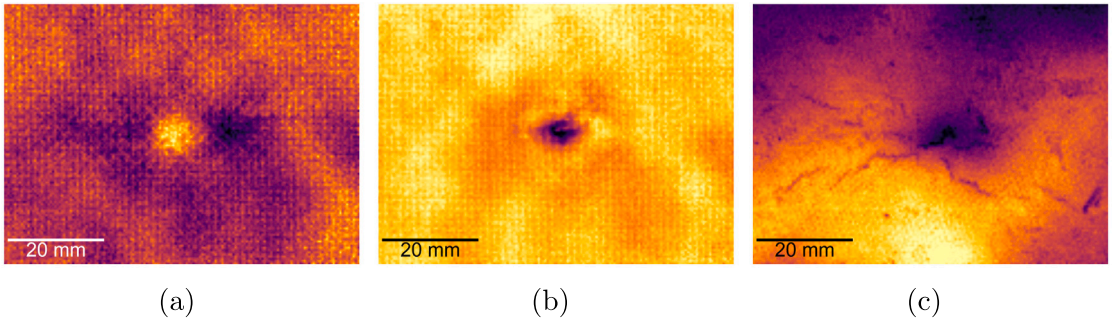


**Fig. 8.** Thermographic images of (a) the front and (b) the back sides of a $[K_8]$ specimen impacted at 115 J, and (c) the front of a $[G_{10}]$ specimen impacted at 86 J.

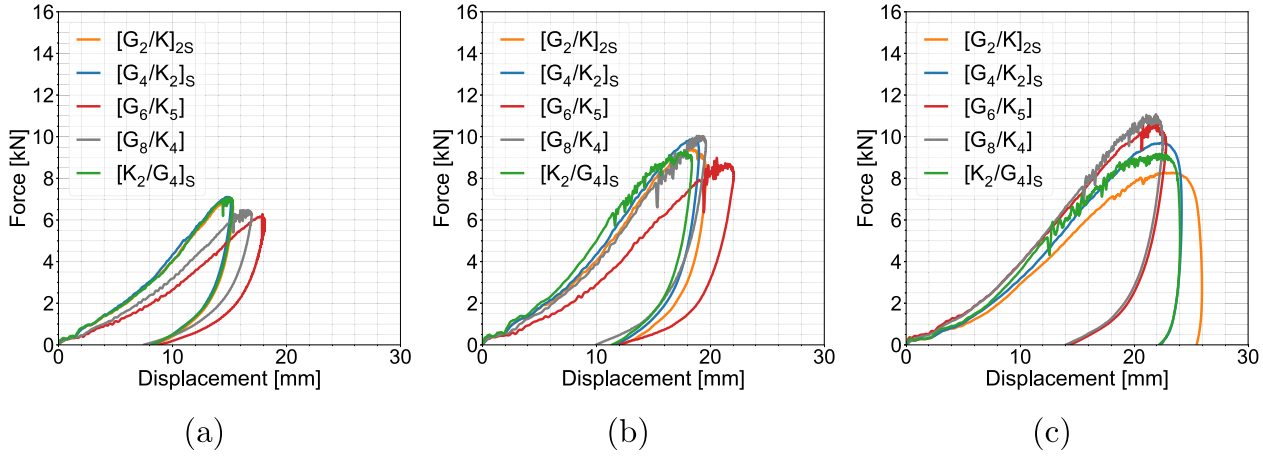


**Fig. 9.** Load vs. displacement curves of the hybrid specimens impacted at (a) 49 J, (b) 86 J, and (c) 115 J.

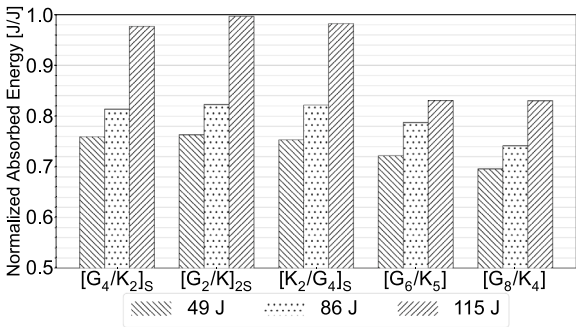


**Fig. 10.** Normalized absorbed energy of hybrid specimens.

In Fig. 9(a) the three symmetric specimens have very similar force vs displacement curves, and the $[G_8/K_4]$ and $[G_6/K_5]$ specimens are less stiff, with lower maximum force and larger maximum displacement. The behavior changes for impact at higher energies; at 86 J the $[G_4/K_2]_S$ and the $[G_8/K_4]$ specimens show the highest force, and the $[G_6/K_5]$ specimen the largest maximum displacement. At 115 J the $[G_8/K_4]$ and the $[G_6/K_5]$ show instead the highest force. The inconsistency in stiffness, maximum force, and displacement is likely due to the different damage mechanisms that depend on the location of the fabrics in the stacking, but the assessment of the repeatability of these results is out of the scope of this paper and will be addressed in future investigation. In the normalized absorbed energy results shown in Fig. 10, it can be observed that the $[G_8/K_4]$ and the $[G_6/K_5]$ specimens absorb significantly less energy than the symmetric specimens, in particular, at 115 J the non-symmetric coupons absorbed approximately 15% less energy. In terms of energy absorption, the non-symmetric specimens outperform the symmetric ones, being capable of bearing higher loads before failure. This behavior differs from that previously reported with epoxy composite, for which symmetric and non-symmetric composites were more alike [21]. The two non-symmetric specimens behave very similarly despite the different aramid ratios, and the absorbed energy is similar to that of the glass specimen even though the areal density is lower, characterizing a positive hybridization effect.

**Table 5**
Summary of the impact results for the hybrid specimens.

| Specimens | | Maximum force [kN] | Maximum displacement [mm] | Absorbed energy [J] | Norm. abs. energy [J/J] |
|---|---|---|---|---|---|
| $[G_4/K_2]_S$ | 49 J | 7.11 | 15.12 | 37.07 | 0.76 |
| | 86 J | 9.87 | 19.01 | 70.43 | 0.82 |
| | 115 J | 9.70 | 24.17 | 110.60 | 0.98 |
| $[G_2/K]_{2S}$ | 49 J | 7.01 | 15.32 | 37.03 | 0.76 |
| | 86 J | 9.41 | 19.63 | 70.37 | 0.82 |
| | 115 J | 8.28 | 25.95 | 112.17 | 1.00 |
| $[K_2/G_4]_S$ | 49 J | 7.07 | 15.28 | 36.54 | 0.75 |
| | 86 J | 9.29 | 18.38 | 70.16 | 0.82 |
| | 115 J | 9.17 | 25.70 | 111.81 | 0.98 |
| $[G_6/K_5]$ | 49 J | 6.29 | 18.06 | 34.79 | 0.72 |
| | 86 J | 8.98 | 22.06 | 68.23 | 0.79 |
| | 115 J | 10.64 | 22.80 | 96.21 | 0.83 |
| $[G_8/K_4]$ | 49 J | 6.48 | 16.94 | 33.70 | 0.70 |
| | 86 J | 10.04 | 19.62 | 63.94 | 0.74 |
| | 115 J | 11.08 | 22.52 | 95.95 | 0.83 |

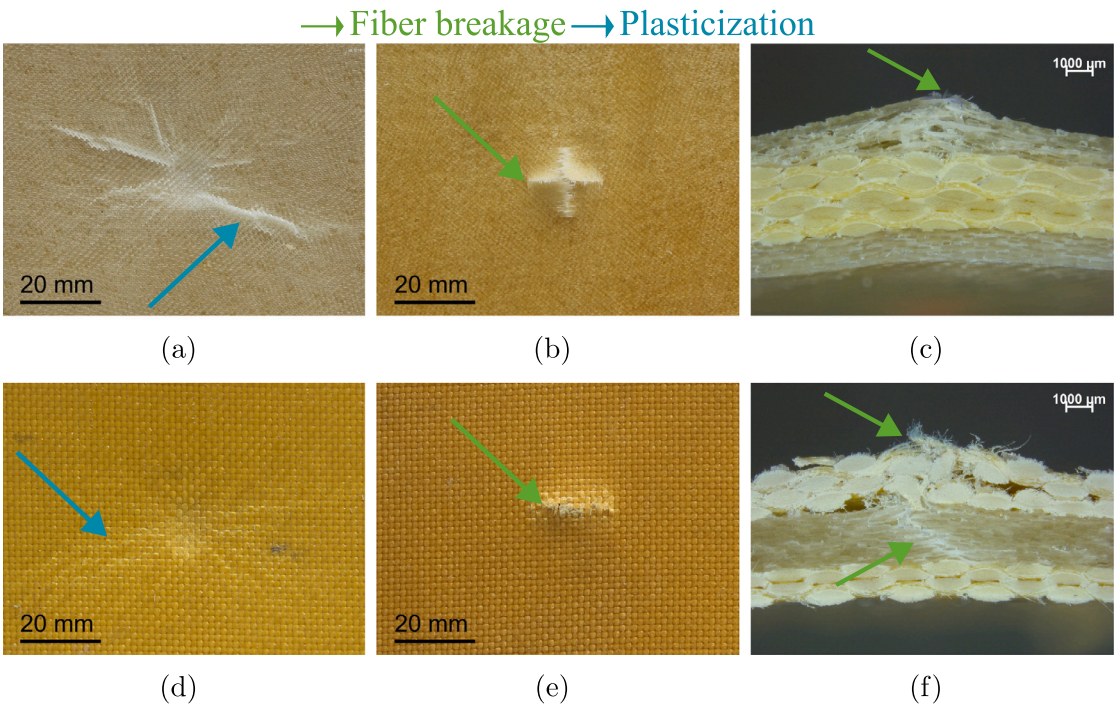


**Fig. 11.** Views of $[G_4/K_2]_S$ and $[K_2/G_4]_S$ specimens impacted at 115 J: (a) front, (b) back, (c) cross-section views of the $[G_4/K_2]_S$ specimen, and (d) front, (e) back, (f) cross-section views of the $[K_2/G_4]_S$ specimen.

The Fig. 11 shows the images of $[G_4/K_2]_S$ and $[K_2/G_4]_S$ specimens tested at 115 J. The front view of the $[G_4/K_2]_S$ specimen in Fig. 11(a) shows a damage mechanism very similar to that in Fig. 7(d) and Fig. A.3(a) for the $[G_{10}]$ and the $[G_{15}]$ specimens, respectively. Severe plasticization appears around the impact area, with yielded matrix in the radial direction. In Fig. 11(b), the cross-shape fracture seen is typical of the back face of impacted composite specimens [21,37]. And Fig. 11(c), highlights that the fiber breakage affects the coupons from the middle plane outwards.

It is reasonable to assume that Kevlar layers play a role in the damage mechanisms, because the crack does not run through the whole thickness, but stops halfway through the specimen section, unlike the $[G_{15}]$. Regarding the damage of $[K_2/G_4]_S$ impacted at 115 J, Fig. 11(d), the damage is identical to the non-hybrid case in Fig. 7(a), while in Fig. 11(e), the back side of the specimen shows different damage compared to that in Fig. 7(b). In this case, the crack runs along the length of the specimen and looks similar to that of $[G_{10}]$ and $[G_{15}]$ specimens.

The hybridization effect is further confirmed in Fig. 11(f), where a crack similar to that reported for the glass specimens is visible in the middle of the specimen, affecting the damage in the outer Kevlar layers too. In terms of absorbed energy and displacement, no significant differences were noticed between the two specimens, while the $[G_4/K_2]_S$ specimen shows 5% larger maximum force.

The $[G_2/K]_{2S}$ specimen impacted at 115 J is displayed in Fig. 12(a–c). The impact side shows radial plasticization, similar to the other specimens with glass layers on the impact side, but the plasticized area is smaller. On the back, the cross-shape fracture is visible, as for the $[G_4/K_2]_S$ specimen, with damage similar to that of the other specimens in this Subsection, i.e., a crack running from the middle of the specimen section outward. This specimen absorbed 100% of the impact energy, 2% more than the other two symmetric specimens.

In Fig. 12(d), the front glass layers of $[G_6/K_5]$ specimen show similar damage to that for glass layers on the impact side, i.e., a large yielded area near the impact area. In Fig. 12(e), fiber pullouts can be seen in the back, similar to the $[K_{13}]$ specimen. Fig. 12(f) shows no cracks or delamination in the front glass layer of the first Kevlar layers, however, fiber breakage and pullouts are visible on the back side, and the outer Kevlar layers present delamination and voids between fabrics tows.

The damage reported for the $[G_6/K_5]$ specimen (not shown here for brevity) is very similar to that of the $[G_8/K_4]$ specimen. In addition, for these two non-symmetric specimens the aramid ratio shows negligible effect in terms of damage mechanisms, and it affects the load vs displacement curves only, for the lower impact energies. The front image is similar to that reported by Rezasefat et al. [22] for a composite with the same reinforcement but an epoxy matrix. However, they reported extensive matrix cracking that is not found in these specimens, due to the higher toughness of the PU thermoset matrix. On the back side, they also reported fiber pullouts; however, the impact bulge and the extent of delamination are much larger for epoxy composites. It is noteworthy that the non-symmetric specimen absorbed almost 20% less energy than the symmetric ones, indicating that this configuration with stiffer glass fabrics facing the impact and Kevlar layers on the back side is capable of absorbing more energy, as reported in previous studies [20,38], by promoting damage mechanisms capable of absorbing a large amount of energy such as plasticization in the front glass layers and fiber breakage and delamination in the rear Kevlar layers.

It is noteworthy that the composites manufactured with PU matrix do not show the v-shape damage region around the impact region, reported for epoxy composites [21,23]. Only for the Kevlar composite in Fig. 7(f), the damage resembles a v-shape. In all other cases, an extended plasticized area characterized the region around the impact, attributed to the higher toughness of this matrix.

The thermographic image of the impact side of $[G_4/K_2]_S$ specimen in Fig. 13(a) highlights the radial plasticized matrix, also, near the dark diagonal mark, an area darker than the surrounding indicates spread matrix damage around the impact. The center of the specimen is very dark because, on the back side, a cross-shape fracture is present. For this reason, the thermographic analysis of the back side is not shown. Fig. 13(b), for the impact side of the $[G_2/K]_{2S}$ specimen, a more localized damage area is seen compared to the $[G_4/K_2]_S$ specimen. The plasticized radial damage in the matrix is barely visible and indicated

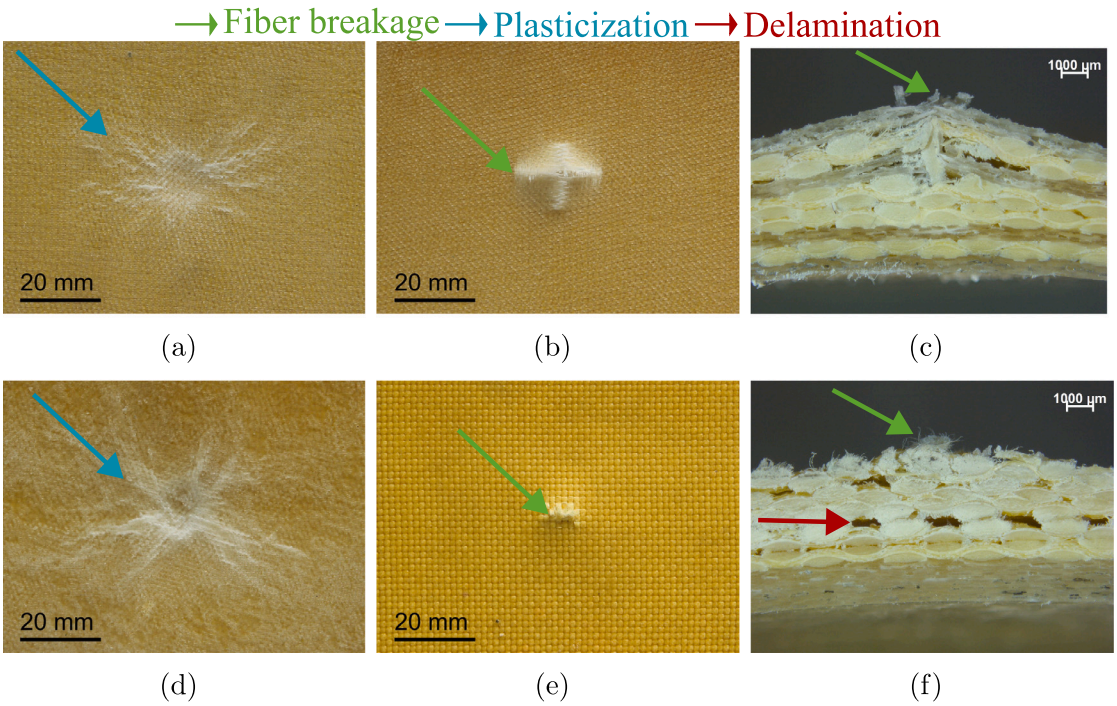


**Fig. 12.** Views of $[G_2/K]_{2S}$ and $[G_6/K_5]$ specimens impacted at 115 J: (a) front, (b) back, (c) cross-section views of the $[G_2/K]_{2S}$ specimen, and (d) front, (e) back, (f) cross-section views of the $[G_6/K_5]$ specimen.

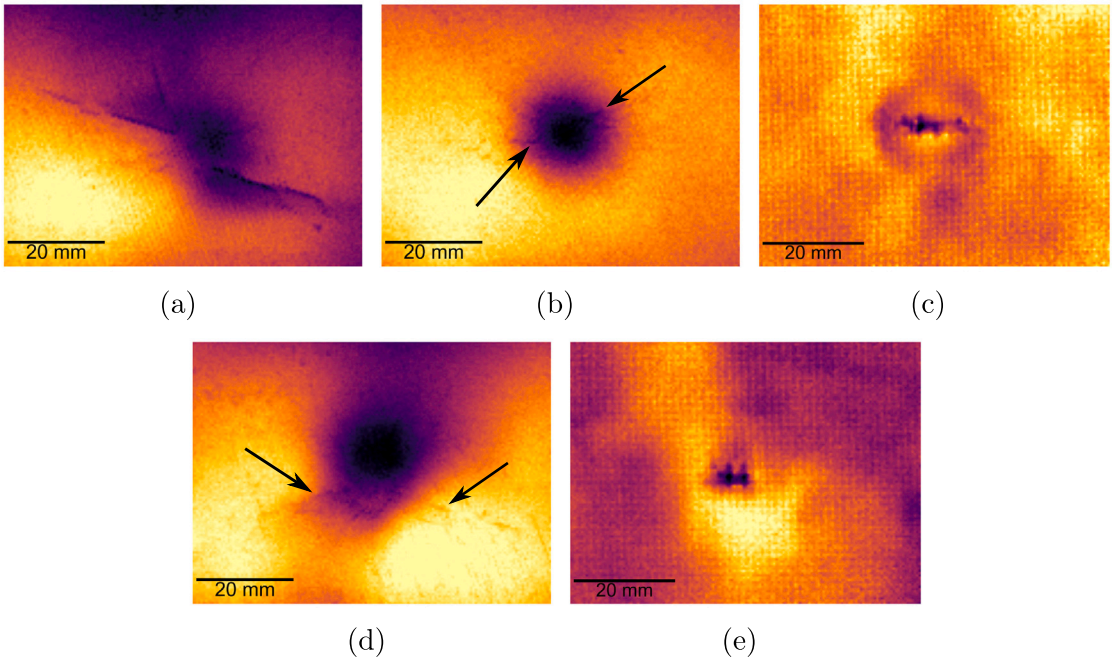


**Fig. 13.** Thermographic images of the front of (a) the $[G_4/K_2]_S$ and (b) the $[G_2/K]_{2S}$ specimens, (c) the back of $[K_2/G_4]_S$ specimen, and (d) the front and (e) the back of $[G_6/K_5]$ specimen, tested at 115 J.

by arrows. In the back of the specimen, the cross-shape fracture is visible, as for the $[G_4/K_2]_S$ specimen. Fig. 13(c) shows the back side of $[K_2/G_4]_S$ specimen, where fiber pullouts are visible in the center. In addition, the circular bulge from the impact is visible near the broken fabric. Fig. 13(d) shows a large damaged area near the impact together with some matrix yielding indicated by the arrows. The back of the specimen in Fig. 13(e) highlights fiber pullouts.

### 3.3. On the effect of the material on the impact face

The experimental load vs displacement curves for non-symmetric hybrid composites are presented in Fig. 14 for the impacts at 49 J, 86 J, and 115 J, using the different materials on the impact side. The normalized absorbed energy is reported in Fig. 15, and in Table 6 the experimental results are summarized.

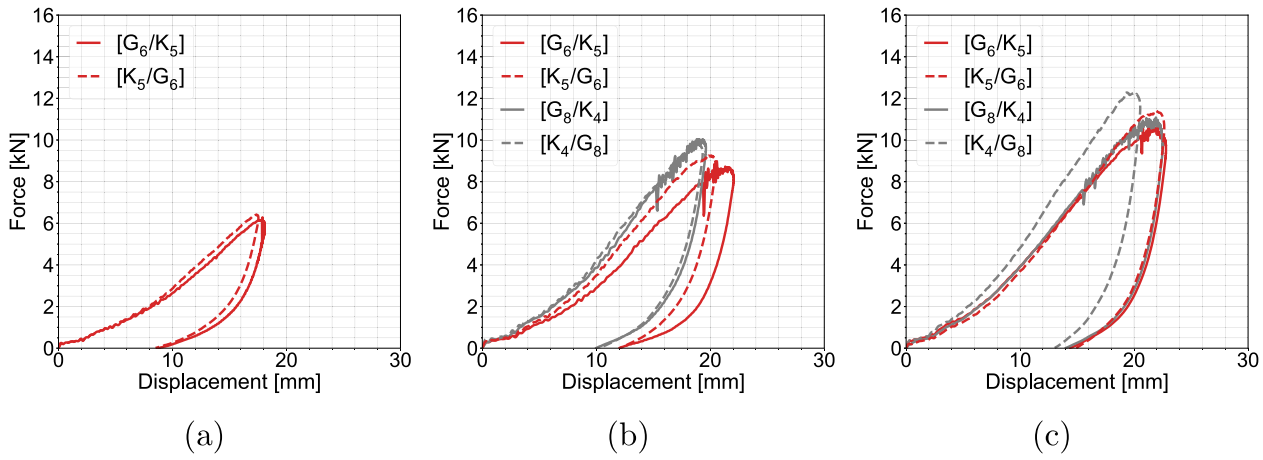


**Fig. 14.** Load vs. displacement curves of the hybrid coupons with Kevlar or glass layers on the side impacted at (a) 49 J, (b) 86 J, and (c) 115 J.

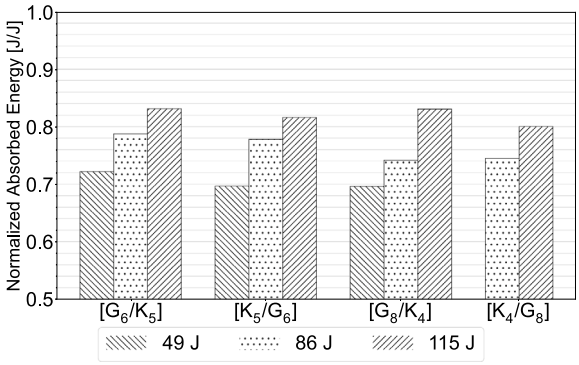


**Fig. 15.** Normalized absorbed energy for hybrid specimens with Kevlar or glass on the impact side.

**Table 6**
Summary of the impact results for the non-symmetric hybrid specimens with Kevlar on the impact side.

| Specimens | | Maximum force [kN] | Maximum displacement [mm] | Absorbed energy [J] | Norm. abs. energy [J/J] |
|---|---|---|---|---|---|
| $[K_5/G_6]$ | 49 J | 6.41 | 17.54 | 33.54 | 0.70 |
| | 86 J | 9.25 | 20.48 | 67.12 | 0.78 |
| | 115 J | 11.41 | 22.65 | 94.21 | 0.82 |
| $[K_4/G_8]$ | 86 J | 9.79 | 19.33 | 64.34 | 0.74 |
| | 115 J | 12.28 | 20.54 | 92.36 | 0.80 |

In terms of stiffness, the effect of different materials on the impact side is quite negligible, except for two cases, i.e., the $[G_6/K_5]$ and the $[G_8/K_4]$ specimens at 86 J and 115 J, respectively, that are stiffer. The force is approximately 4% higher when Kevlar is on the impact side, and the displacement is 4% smaller, whereas the specimens with glass layers on the impact side tend to absorb slightly greater energy ($\sim 4\%$), contrary to what was reported by Rezasefat et al. for the glass-aramid epoxy composites [22].

It is important to highlight that the force vs displacement curves, reported in Figs. 4, 5, 9, and 14, did not show the typical oscillating behavior reported for low-velocity impact tests [39], including composites with the same fibers in an epoxy matrix [21]. It is important to mention that the difference is not caused by the low pass filter applied by the testing machine since the same acquisition technique was adopted in [21], rather by the damping properties of the PU matrix employed in this study, even though significant oscillation is noted at high force and large displacement, when fiber breakage occurs, e.g., the $[K_8]$ specimen impacted at 86 J in Fig. 4(b). These features are common to all specimens reported in the current study.

Fig. 16 displays the $[K_5/G_6]$ specimen impacted at 115 J. The $[K_4/G_8]$ specimen is not shown because the damage is very similar. Fig. 16(a) shows the same radial damage due to matrix plasticization reported for specimens with Kevlar on the impact side, e.g., Fig. 7(d) and Fig. 11(d); while the back of the specimen in Fig. 16(b) shows no damage. In Fig. 16(c), showing the cross-section view, no damage in the fabrics nor delamination is visible.

Fig. 17 displays the thermographic image of the impact side of the same $[K_5/G_6]$ specimen. The impact location is visible and highlighted by a dashed line, while the surrounding lighter area indicates the plasticized area. The thermographic analysis of the back side is not reported because no damage is seen. From these results, it can inferred that this configuration absorbs most of the energy by matrix yielding and plasticization. Instead, when glass is on the impact side, the kevlar layers on the back side tend to fail and fiber pullout is visible. This can also be seen in the load vs displacement curves since no oscillation related to the fiber breakage is present. The difference in damage mechanisms could also explain the difference in absorbed energy since fiber breakage absorbs energy in the process.

## 4. Conclusion

In this study low-velocity impact tests were carried out on different configurations of specimens, produced using plain-weave Kevlar 29 and 8-harness satin S2-glass fabrics as reinforcements, and an elastomeric polyurethane as matrix. First, four Kevlar and glass specimens with varying thicknesses were tested, to highlight specific features of the damage mechanisms of the two types of specimens and to obtain benchmark values for maximum force and displacement, and absorbed energy. Then symmetric and non-symmetric hybrid specimens with different stacking sequences were investigated. Thermal non-destructive testing using an IR camera was carried out to enrich the analyses of the damage mechanisms and highlight damage features. The main findings and conclusions are summarized below.

- The Kevlar and glass coupons showed large matrix yielding and plasticization on the front surface, while, on the back, fiber breakage and pullouts characterized glass and Kevlar specimens, respectively.

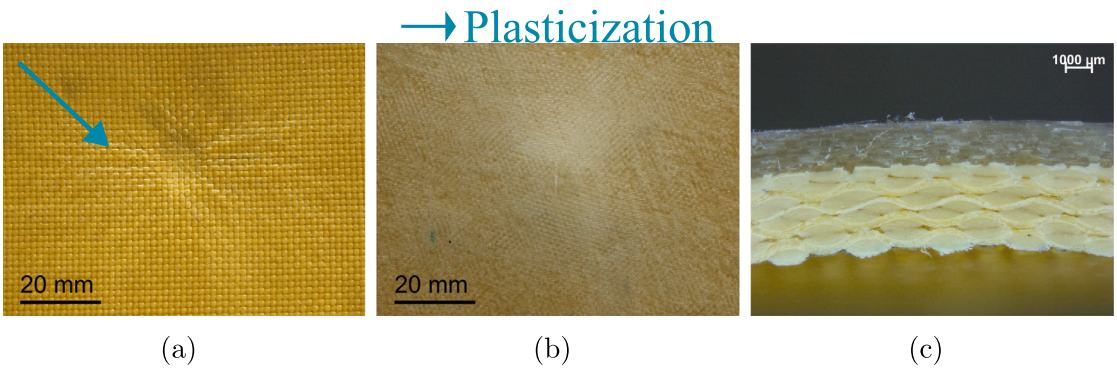


**Fig. 16.** (a) Front, (b) back, and (c) cross-section views of $[K_5/G_6]$ specimen impacted at 115 J.

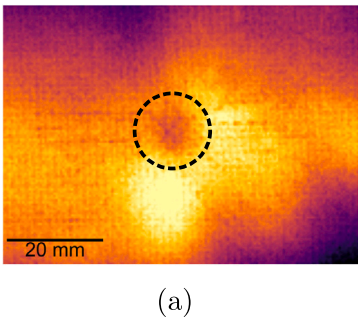


**Fig. 17.** Thermographic image of the front of $[K_5/G_6]$ specimen impacted at 115 J.

- The hybrid specimens showed characteristics from both types of specimens, including large plastic deformation on the front surface. The specimens with glass fabric on the back layers showed cross-shaped fiber breakage, while those with Kevlar, showed fiber pullouts.
- For the non-symmetric specimens, fiber pullouts appeared when Kevlar layers were on the back side, while a large bulge was reported for glass layers on the back side, without fiber breakage.
- The Kevlar specimens absorbed slightly more energy than the glass ones, while a large difference was found between symmetric and non-symmetric hybrids, and the symmetric specimens absorbed much more energy at higher impact energy. For the non-symmetric specimens, the energy absorbed by those with glass on the impact side was slightly larger.

The findings of this study have unveiled potential benefits that deserve more in-depth exploration, particularly concerning the adoption of elastomeric PU resins for absorbing larger amounts of energy compared to traditional epoxy. The results also indicate the feasibility of designing composite structures with reduced vulnerability to delamination.

The overall behavior showed by the specimens investigated in this work is interesting and promising for possible application in the field of protection, and perhaps also for structural application, considering the high fracture toughness of the matrix. However, the adopted experimental fixture should be further investigated, and a single fixture designed to investigate the stiffer epoxy and the softer PU composite, keeping the same boundary conditions, can enlighten the beneficial effects of elastomeric PU resins for low-velocity impacts.

## CRediT authorship contribution statement

**Alessandro Vescovini:** Conceptualization, Data curation, Investigation, Methodology, Writing – original draft. **Joziel A. Cruz:** Conceptualization, Investigation, Methodology, Writing – review & editing. **Dayou Ma:** Conceptualization, Investigation, Methodology, Writing – review & editing. **Chiara Colombo:** Conceptualization, Methodology, Writing – review & editing. **Antonio Salerno:** Conceptualization, Methodology, Writing – review & editing. **Otavio Bianchi:** Conceptualization, Investigation, Methodology, Writing – review & editing. **Sandro C. Amico:** Conceptualization, Funding acquisition, Methodology, Supervision, Writing – review & editing. **Andrea Manes:** Conceptualization, Funding acquisition, Supervision, Writing – review & editing.

## Data availability

Data will be made available on request.

## Acknowledgments

The authors affiliated with UFRGS would like to acknowledge the support from CNPq and CAPES. The first author acknowledges Carlo Cogliati for his support in conducting the experimental campaign.

## Declaration of competing interest

The authors declare that they have no known competing financial interests or personal relationships that could have appeared to influence the work reported in this paper.

## Appendix. Additional images of tested specimens

See Figs. A.1–A.3.

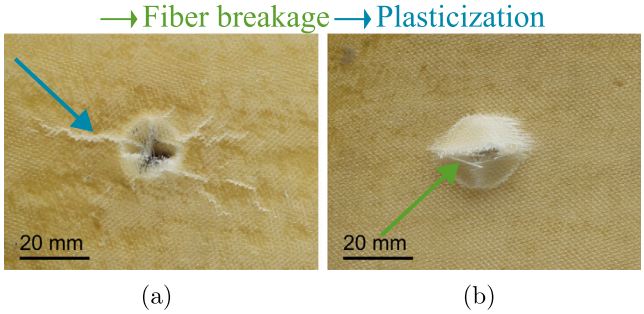


**Fig. A.1.** (a) Front and (b) back views of $[G_{10}]$ specimen tested at 115 J.

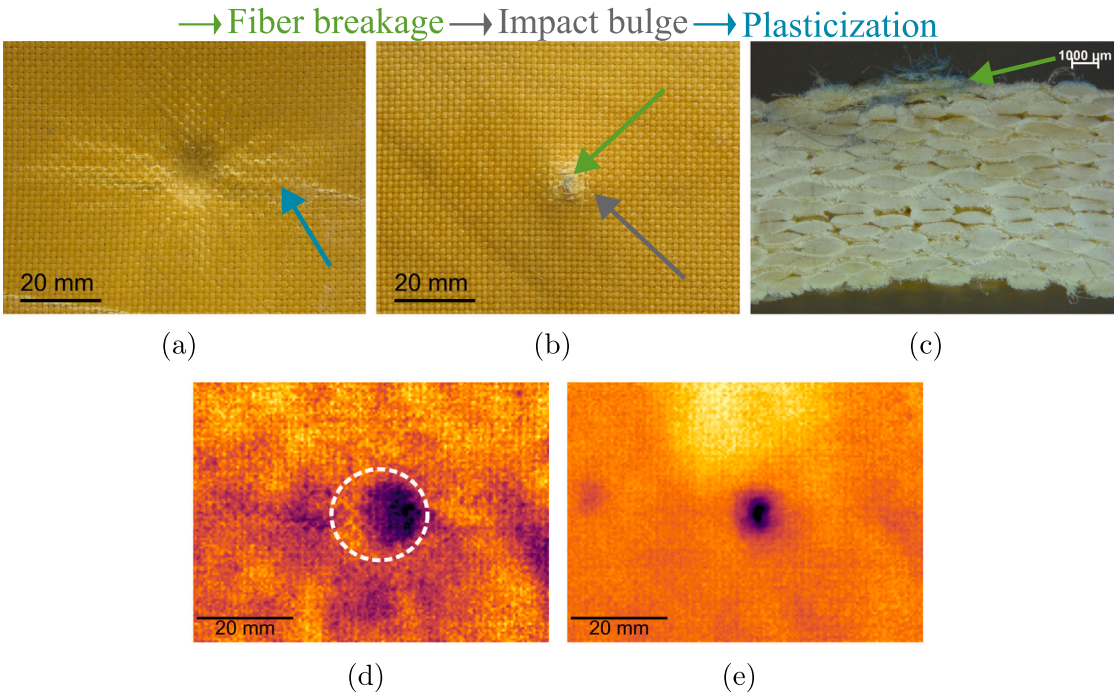


**Fig. A.2.** (a) Front, (b) back, and (c) cross-section views and (d) front and (e) back thermography images of $[K_{13}]$ specimen tested at 115 J.

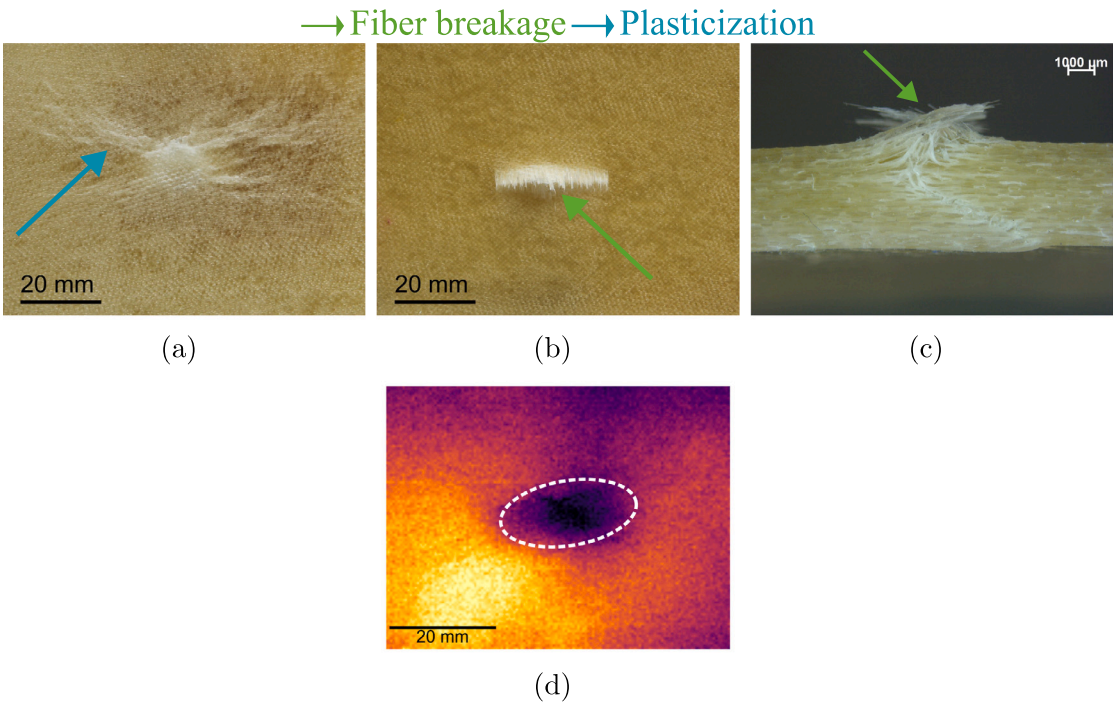


**Fig. A.3.** (a) Front, (b) back, (c) cross-section, and (d) front thermography views of $[G_{15}]$ specimen tested at 115 J.

## References

[1] R. Bogenfeld, J. Kreikemeier, T. Wille, Review and benchmark study on the analysis of low-velocity impact on composite laminates, Eng. Fail. Anal. 86 (2018) 72–99, http://dx.doi.org/10.1016/j.engfailanal.2017.12.019.

[2] S. Shah, S. Karuppanan, P. Megat-Yusoff, Z. Sajid, Impact resistance and damage tolerance of fiber reinforced composites: A review, Compos. Struct. 217 (2019) 100–121, http://dx.doi.org/10.1016/j.compstruct.2019.03.021.

[3] R. Karakuzu, B. Algan, M.E. Deniz, Effects of specimen dimensions and impact energy on energy absorption and damage of glass/epoxy composite plates, Mater. Test. 61 (3) (2019) 231–238, http://dx.doi.org/10.3139/120.111309.

[4] H.E. Yalkın, R. Karakuzu, T. Alpyıldız, Experimental and numerical behaviors of gfrp laminates under low velocity impact, J. Composite Mater. 54 (21) (2020) 2999–3007, http://dx.doi.org/10.1177/0021998320906871.

[5] M. Hosur, M. Adbullah, S. Jeelani, Studies on the low-velocity impact response of woven hybrid composites, Compos. Struct. 67 (3) (2005) 253–262, http://dx.doi.org/10.1016/j.compstruct.2004.07.024, Dynamic Response of Advanced Materials and Structures.

[6] Y. Swolfs, L. Gorbatikh, I. Verpoest, Fibre hybridisation in polymer composites: A review, Composites A 67 (2014) 181–200, http://dx.doi.org/10.1016/j.compositesa.2014.08.027.

[7] M. Sayer, N.B. Bektaş, O. Sayman, An experimental investigation on the impact behavior of hybrid composite plates, Compos. Struct. 92 (5) (2010) 1256–1262,

http://dx.doi.org/10.1016/j.compstruct.2009.10.036.
[8] E. González, P.M.J. Sainz de Aja, P. Cruz, P. Camanho, Effects of interply hybridization on the damage resistance and tolerance of composite laminates, Compos. Struct. 108 (2014) 319–331, http://dx.doi.org/10.1016/j.compstruct.2013.09.037.
[9] A. Wagih, T. Sebaey, A. Yudhanto, G. Lubineau, Post-impact flexural behavior of carbon-aramid/epoxy hybrid composites, Compos. Struct. 239 (2020) 112022, http://dx.doi.org/10.1016/j.compstruct.2020.112022.
[10] C. Zhang, Y. Rao, W. Li, Low-velocity impact behavior of intralayer hybrid composites based on carbon and glass non-crimp fabric, Compos. Struct. 234 (2020) 111713, http://dx.doi.org/10.1016/j.compstruct.2019.111713.
[11] M. Kazemi, L. Shanmugam, A. Dadashi, M. Shakouri, D. Lu, Z. Du, Y. Hu, J. Wang, W. Zhang, L. Yang, J. Yang, Investigating the roles of fiber, resin, and stacking sequence on the low-velocity impact response of novel hybrid thermoplastic composites, Composites B 207 (2021) 108554, http://dx.doi.org/10.1016/j.compositesb.2020.108554.
[12] A.K. Barouni, H.N. Dhakal, Damage investigation and assessment due to low-velocity impact on flax/glass hybrid composite plates, Compos. Struct. 226 (2019) 111224, http://dx.doi.org/10.1016/j.compstruct.2019.111224.
[13] A.K.J. Al-Shamary, R. Karakuzu, H. Kandas, O. Ozdemir, Experimental investigation of the impact behavior of glass/epoxy composite materials with the natural fiber layer, Mater. Test. 64 (6) (2022) 780–786, http://dx.doi.org/10.1515/mt-2021-2133.
[14] S. Ahmed, X. Zheng, L. Yan, C. Zhang, X. Wang, Influence of asymmetric hybridization on impact response of 3D orthogonal woven composites, Compos. Sci. Technol. 199 (2020) 108326, http://dx.doi.org/10.1016/j.compscitech.2020.108326.
[15] I. Papa, L. Boccarusso, A. Langella, V. Lopresto, Carbon/glass hybrid composite laminates in vinylester resin: Bending and low velocity impact tests, Compos. Struct. 232 (2020) 111571, http://dx.doi.org/10.1016/j.compstruct.2019.111571.
[16] M. Aktas, R. Karakuzu, B.M. Icten, Impact behavior of glass/epoxy laminated composite plates at high temperatures, J. Compos. Mater. 44 (19) (2010) 2289–2299, http://dx.doi.org/10.1177/0021998310369576.
[17] R. Karakuzu, A. Djele, A. Dogan, High temperature effect on quasi-static and low velocity impact behaviors of advanced composite materials, Proc. Inst. Mech. Eng. C 235 (23) (2021) 7110–7119, http://dx.doi.org/10.1177/09544062211007169.
[18] A.A.X. da Silva, J.A. Souza, A. Manes, S.C. Amico, In-plane permeability and mechanical properties of R-glass/aramid hybrid composites, J. Mater. Eng. Perform. 29 (7) (2020) 4484–4492, http://dx.doi.org/10.1007/s11665-020-04944-1.
[19] A.A.X. da Silva, R. Scazzosi, A. Manes, S.C. Amico, High-velocity impact behavior of aramid/S2-glass interply hybrid laminates, Appl. Compos. Mater. (2021) http://dx.doi.org/10.1007/s10443-021-09946-3.
[20] A. Vescovini, L. Balen, R. Scazzosi, A. da Silva, S. Amico, M. Giglio, A. Manes, Numerical investigation on the hybridization effect in inter-ply S2-glass and aramid woven composites subjected to ballistic impacts, Compos. Struct. 276 (2021) 114506, http://dx.doi.org/10.1016/j.compstruct.2021.114506.
[21] M. Rezasefat, A. Gonzalez-Jimenez, D. Ma, A. Vescovini, L. Lomazzi, A.A. da Silva, S.C. Amico, A. Manes, Experimental study on the low-velocity impact response of inter-ply S2-glass/aramid woven fabric hybrid laminates, Thin-Walled Struct. 177 (2022) 109458, http://dx.doi.org/10.1016/j.tws.2022.109458.
[22] M. Rezasefat, D. Ma, A.A. da Silva, C. Colombo, S.C. Amico, M. Giglio, A. Manes, Multi-criteria decision-making analysis and numerical simulation of the low-velocity impact response of inter-ply S2-glass/aramid woven fabric hybrid laminates, Compos. Struct. 312 (2023) 116867, http://dx.doi.org/10.1016/j.compstruct.2023.116867.
[23] B. Vieille, V. Casado, C. Bouvet, About the impact behavior of woven-ply carbon fiber-reinforced thermoplastic- and thermosetting-composites: A comparative study, Compos. Struct. 101 (2013) 9–21, http://dx.doi.org/10.1016/j.compstruct.2013.01.025.
[24] H.-W. Engels, H.-G. Pirkl, R. Albers, R.W. Albach, J. Krause, A. Hoffmann, H. Casselmann, J. Dormish, Polyurethanes: Versatile materials and sustainable problem solvers for today's challenges, Angew. Chem., Int. Ed. Engl. 52 (36) (2013) 9422–9441, http://dx.doi.org/10.1002/anie.201302766.
[25] J.A. Cruz, E.F. Kerche, O. Bianchi, A. Manes, S.C. Amico, Castor oil-based polyurethane/S2 glass/aramid hybrid composites manufactured by vacuum infusion, Polymers 14 (23) (2022) http://dx.doi.org/10.3390/polym14235150.
[26] Z. Zhao, H. Lin, P. Ma, Low-velocity impact damage simulation of biaxial warp-knitted flexible composite with simplified microstructure model, Appl. Compos. Mater. (2022) http://dx.doi.org/10.1007/s10443-022-10036-1.
[27] J. Nicholas, M. Mohamed, G. Dhaliwal, S. Anandan, K. Chandrashekhara, Effects of accelerated environmental aging on glass fiber reinforced thermoset polyurethane composites, Composites B 94 (2016) 370–378, http://dx.doi.org/10.1016/j.compositesb.2016.03.059.
[28] J.A. Cruz, S.C. Amico, O. Bianchi, Effect of the aramid pulp on the physicochemical, viscoelastic properties and rheokinetics of polyurethanes, J. Polymer Res. 30 (2022) http://dx.doi.org/10.1007/s10965-022-03393-9.
[29] Dupont, Kevlar® aramid fiber technical guide, 2017, URL https://www.dupont.com/.
[30] Hexcel, Hexforce™ 6781 datasheet, 2022, URL https://www.hexcel.com/.
[31] ASTM D7136/D7136M - 15 standard test method for measuring the damage resistance of a fiber-reinforced polymer matrix composite to a drop-weight impact event, 2015.
[32] A.H. Astaraee, A. Salerno, S. Bagherifard, P. Carlone, H. Parmar, A. Astarita, A. Viscusi, C. Colombo, Thermographic analysis of composite metallization through cold spray, Metals 11 (11) (2021) http://dx.doi.org/10.3390/met11111860.
[33] E.A. Abdallah, C. Bouvet, S. Rivallant, B. Broll, J.-J. Barrau, Experimental analysis of damage creation and permanent indentation on highly oriented plates, Compos. Sci. Technol. 69 (7) (2009) 1238–1245, http://dx.doi.org/10.1016/j.compscitech.2009.02.029.
[34] R. Olsson, Analytical prediction of large mass impact damage in composite laminates, Composites A 32 (9) (2001) 1207–1215, http://dx.doi.org/10.1016/S1359-835X(01)00073-2.
[35] I. Choi, Geometrically nonlinear transient analysis of composite laminated plate and shells subjected to low-velocity impact, Compos. Struct. 142 (2016) 7–14, http://dx.doi.org/10.1016/j.compstruct.2016.01.070.
[36] K. Giasin, H.N. Dhakal, C.A. Featheroson, D.Y. Pimenov, C. Lupton, C. Jiang, A. Barouni, U. Koklu, Effect of fibre orientation on impact damage resistance of S2/FM94 glass fibre composites for aerospace applications: An experimental evaluation and numerical validation, Polymers 14 (1) (2022) http://dx.doi.org/10.3390/polym14010095.
[37] A.K. Bandaru, S. Patel, S. Ahmad, N. Bhatnagar, An experimental and numerical investigation on the low velocity impact response of thermoplastic hybrid composites, J. Compos. Mater. 52 (7) (2018) 877–889, http://dx.doi.org/10.1177/0021998317714043.
[38] B. Jang, L. Chen, C. Wang, H. Lin, R. Zee, Impact resistance and energy absorption mechanisms in hybrid composites, Compos. Sci. Technol. 34 (4) (1989) 305–335, http://dx.doi.org/10.1016/0266-3538(89)90002-X.
[39] M. Salvetti, A. Gilioli, C. Sbarufatti, A. Manes, M. Giglio, Analytical model of the dynamic behaviour of CFRP plates subjected to low-velocity impacts, Composites B 142 (2018) 47–55, http://dx.doi.org/10.1016/j.compositesb.2018.01.005.